Computers and Structures 299 (2024) 107369

Contents lists available at ScienceDirect

Computers and Structures

journal homepage: www.elsevier.com/locate/compstruc

A displacement-based finite element formulation for solving elastic wave problems in coupled fluid-solid media on a GPU

Yiannis Simillides [a,*], Peter Huthwaite [a,*], Michał K. Kalkowski [b], Michael J.S. Lowe [a]

[a] Department of Mechanical Engineering, Imperial College London, UK
[b] Institute of Sound and Vibration Research, University of Southampton, UK

ARTICLE INFO

Keywords:
Ultrasound
Fluid-structure interaction
Finite element method (FE)
Graphical processing units (GPU)
Underwater acoustics
Non-destructive testing (NDT)

ABSTRACT

Ultrasonic wave propagation and scattering involving both solids and fluids underpins many key configurations in non-destructive testing and underwater acoustics. The resulting interactions are highly dependent on both material parameters and geometries and are difficult and expensive to investigate experimentally. Modelling capabilities are often used to overcome this, but these are also complex and computationally expensive due to the complexity of the fluid-solid interactions. We introduce a novel explicit time-domain finite element method for simulating ultrasonic waves interacting with fluid-solid interfaces. The method is displacement-based, and relies on classical hourglassing control, in addition to a modified time-stepping scheme to damping out shear motion in an inviscid fluid. One of the key benefits of the displacement-based approach is that nodes in the fluid have the same number of degrees of freedom as those in the solid. Therefore defining a fluid-solid model is as easy as defining an all-fluid or all-solid model, avoiding the need for any special treatments at the interfaces. It is thus compatible with typical elastodynamic finite element formulations and ready for implementation on a graphical processing unit. We verified the method across a range of problems involving millions of degrees of freedom in fields such as non-destructive testing and underwater acoustics.

1. Introduction

Ultrasonic propagation in domains composed of both solids and fluids is a key area of interest in diverse subject areas such as: medical [1], geophysics [2], non-destructive testing, engineering [3] or underwater acoustics [4]. Key use cases are those of immersion testing [5], pipe inspection [6], and scattering from underwater objects [7]. Numerical models are needed to accurately simulate ultrasonic wave phenomena in coupled solid-fluid interactions for a range of complex geometries and materials in such real-world applications, as analytical or experimental methods can be restricted to simple configurations or limited to a small subset of parameters. Numerical methods, such as the Finite Element (FE) method, are often used to handle complex geometries by coupling solid and fluid domains using a pressure-based formulation within the fluid [8], linked to the conventional displacement-based formulation in the solid However, this typically requires more complex matrix processing which can be computationally expensive and not always feasible. In addition, such computations are rarely able to take advantage of the acceleration capability of highly-parallel computing hardware such as GPUs (Graphical Processing Units) due to their implicit nature, relying on matrix inversions. Explicit methods are preferred to implicit methods for GPU calculations, as the variables at one time-step can be computed from their known values at previous time-steps. The reason for this preference is the large number of processors which allow many threads to run in parallel as well as the GPUs high memory bandwidth for loading in data. This is well known in the literature, as can be seen in [9], where it is stated that “explicit methods map well to the GPU architecture as the output elements can be computed independently of each other, thus making full use of the high computing throughput of a GPU” or in [10], where an in-depth explanation of the GPU architecture and how this maps to explicit-in-time finite elements methods is given and the reader is referred to these for further information about the GPU architecture.

Due to the complexities and prominence of the problem, significant research work has been carried out to improve modelling capabilities for ultrasonic wave propagation and scattering, using both analytical and numerical methods. In the analytical framework, mathematical solutions exist for some geometries. For example, Faran [11] investigated sound scattering from solid cylinders and spheres in liquid. At the time, this work was limited by the numerical evaluation of the Bessel func-

---

* Corresponding authors.
E-mail address: y.simillides18@imperial.ac.uk (Y. Simillides).

https://doi.org/10.1016/j.compstruc.2024.107369
Received 8 January 2024; Accepted 25 March 2024

tions, but this poses no problems with modern computing capabilities. In [7] by Skelton and James, results are presented for scattering patterns for layered media in cylindrical and spherical domains. Analytical results are generally limited to simple geometries, which are not able to represent realistic practical scenarios often involving complex configurations.

Despite invaluable physical insights offered by the analytical models, only numerical methods enable a full range of complex, industry-relevant configurations to be simulated. Numerical experiments allow both researchers and practitioners to perform multiple simulations in order to develop new approaches or methods and to validate processing of results before carrying out more complex and expensive experimental tests. The numerical models can further be used to model physical phenomena and to evaluate different types of defect in parametric studies, which are not possible to do in a consistent manner experimentally, or to assist with sensor design and placement [12].

A multitude of numerical techniques have been used to accurately predict some of the properties of ultrasound wave characteristics in solid and fluid materials. The finite-difference (FD) method has frequently been used throughout the literature, due to its comparative ease of use and low computational power required. Unfortunately, without significant modification, it can not accurately model complex domains because it is restricted to modelling on a uniformly spaced grid. Important contributions to the application of the FD method to wave propagation in solid-fluid media can be found in [13] where they accurately modelled the Scholte wave [14] or [15] who modelled elastic wave propagation in submerged solids. In [4], an FD method in polar coordinates was used to calculate the response from submerged cylinders with an arbitrary amount of filling, which is not possible using conventional axisymmetric techniques. However, the difficulty in handling complex geometries or configurations remains a fundamental drawback.

Other techniques used in the literature are the transfer matrix method (TMM) [16] with associated disadvantages at smaller frequencies [17], the distributed point source method (DPSM) [18] or the boundary element method (BEM) [19]. Extensive work has also been undertaken on combining different methods, such as in [20] where a boundary element method is used to model the fluid which is then coupled with a finite element (FE) method for the solid or in [21] where an analytical solution for the fluid is combined with an FE method for the solid.

In the FE literature for the fluid-structure interaction (FSI), various formulations have been proposed to model the acoustic wave propagation. Most common are the pressure formulation or the velocity potential formulation [22], which have the benefit of only requiring one degree of freedom (DoF) per node. There have also been attempts with non-standard elements, such as the Raviart-Thomas elements which are edge-based and do not seem to suffer from hourglassing [23]. Hourglassing is the phenomenon where certain non-physical modes remain stressless and they quickly dominate and cause instability in the solution [24]. Despite showing much promise, the Raviart-Thomas elements are not compatible with existing FE software or procedures such as meshing. Coupling solid and fluid domains using a pressure-based formulation in FE results in a matrix inversion, which is computationally expensive. This matrix operation is not always feasible, especially for large problems. Such industry-relevant cases involving only solid media can be solved using highly-efficient displacement-based elastodynamic FE solvers benefiting from graphical computing cards [10]. Unfortunately, the pressure-based formulation cannot be used in that framework because of the aforementioned matrix inversion and the required special treatment as the solid-fluid boundary.

The displacement-based formulation for fluids may be the way forward but it was troubled by its own challenges in the past. Most reported problems include added computational requirements when compared to pressure-based formulations, as it is a vector-based quantity compared to the scalar pressure, and the presence of spurious circulation modes [25]. These spurious circulation modes can be found throughout the numerical method literature and extensive research has been carried out to control these instabilities, such as by Hamdi [26] who applied a penalty method, by Belytschko who used mesh stabilisation techniques [24] or Bathe [27] who used a mixed method. Unfortunately, these are often not suitable for GPU calculations due to the added mathematical terms, which result in non-symmetric or non-sparse matrices.

To improve the versatility of time-domain finite element modelling in coupled fluid-solid media, we propose developing a displacement-based FE formulation designed for use on a GPU. This means the method is explicit-in-time and relies on a modified damping matrix to minimise any non-physical shear motion in the fluid. In addressing the concerns mentioned above, we have relied on the classical hourglass control. Our development draws from the work done by Chen [25] on reduced integration techniques for four-noded quadrilateral elements to reduce hourglassing, and Everstine [28] who configures an isotropic elastic solid to represent a compressible inviscid fluid. Our proposed formulation enables applying the time domain finite element method in coupled media to problems of industrial scale. The method's versatility for time-domain problems, which allow us to extract data for multiple frequencies from one simulation and its ability to handle arbitrary and complex geometries, is crucial to the problems we are considering. Furthermore, it can handle problems from diverse domains, which often have very different scales of interest. For example, in [29], objects of 1 mm radius with frequencies up to 3 MHz were investigated, whereas in [4] objects of 1 m radius with frequencies of 1 kHz were investigated. Designing the formulation with the hardware in mind is essential for enabling simulation of realistic configurations. The GPU acceleration enables models to be set up and solved at extremely high speed. This allows for executing simulations involving hundreds of millions of degrees of freedom in a relatively short time, enabling fine mesh refinement or performing parametric studies efficiently. While the displacement-based formulation adds 1 (in 2D) or 2 (in 3D) extra degrees of freedom to the nodes in the fluid domain compared to a scalar (e.g. pressure-based) formulation the displacement-based methods result in symmetric, sparse matrices, whereas pressure based formulations after treatment at the boundary can result in non-symmetric and dense matrices. The non-symmetry and need for matrix inversion also pose significant challenges to GPU implementation. We are no longer guaranteed a sparse matrix; this results in a significant amount of increased memory and storage, and as we are often bandwidth limited, as discussed in [10], this can drastically slow down calculations, introducing additional bottlenecks. A displacement-based formulation ensures compatibility with existing solid solvers, alongside a non-diagonal damping matrix that is suitable for GPU calculations and does not produce (significant) hourglassing. Thus due the increased performance of the GPUs means we can solve similarly sized problems faster for a required accuracy. The results we present throughout this paper are in 2D and for inviscid fluids, although we expect the method to generalise well to both 3D simulations and viscous fluids, although these should be properly validated before use.

The structure of the remainder of the paper is as follows. Challenges of the fluid-solid interaction problem will be described in Section 2. The FE formulation of both solid and fluid will be given in Section 2.1. Numerical results, such as scattering patterns, dispersion curves, attenuation and wave velocity, will be compared with existing solutions and methods and will be provided in Section 4 with a brief conclusion in Section 5.

2. Problem formulation

The first challenge when modelling the FSI using conventional pressure-based methods is the continuity on the boundary between the solid and the fluid. By describing the fluid using the same variable as we use in the solid, i.e. displacement, continuity (of the variable) across the boundary is automatically achieved as we do not need to convert to a different variable.

2.1. Finite element formulation

We begin by introducing the basics of the finite element method but do not cover these in detail as FE is a classical and established numerical method and the reader is referred to works such as [30–32] for full details. The majority of finite element software implementations such as [10,32] have the following structure. First we create and discretise the area of interest into finite elements, using a meshing algorithm. Then, we assemble local matrices on each element and use a local-to-global mapping to assemble the matrices. Finally, we solve the resulting system of equations.

The linear wave equation has the following spatial FE formulation [33]

$$\boldsymbol{K}\boldsymbol{u} + \boldsymbol{C}\dot{\boldsymbol{u}} + \boldsymbol{M}\ddot{\boldsymbol{u}} = \boldsymbol{f}, \tag{1}$$

where $\boldsymbol{u}$ is the displacement vector and $\dot{\boldsymbol{u}}$, $\ddot{\boldsymbol{u}}$ are the first and second derivatives with respect to time respectively, $\boldsymbol{K}, \boldsymbol{C}, \boldsymbol{M}$ are the stiffness, damping and mass matrices respectively and $\boldsymbol{f}$ is the forcing vector.

2.1.1. Finite element formulation for solid materials

FE formulations for displacement-based solid elements are well-known [34] and are briefly discussed below so that we can introduce the necessary changes made for fluid materials. The element stiffness matrix $\boldsymbol{K}^e$, where the superscript is to denote "local element", of an element is given as [34]

$$\boldsymbol{K}^e = \int \boldsymbol{B}^T \boldsymbol{E} \boldsymbol{B} \, \mathrm{d}V. \tag{2}$$

The matrix $\boldsymbol{B}$ in Equation (2) is the strain-displacement matrix which comes from the strain-displacement formula

$$\epsilon = \boldsymbol{B}\boldsymbol{u}. \tag{3}$$

These can be found in the literature [35] and depend on the choice of the element, for which further information will be provided in Section 2.1.2. The matrix $\boldsymbol{E}$ is the stress-strain matrix which depends on the material parameters. For convenience for the development of the fluid element the stress-strain matrix $\boldsymbol{E}$ for a 2D isotropic solid is shown, although due to the displacement-based nature of our approach, the fluid formulation will work with solids that are isotropic or anisotropic of any symmetry. Furthermore, this derivation should also hold true for 3D modelling since no specific simplifications were assumed for the 2D case, although verification and validation studies should be carried out in the 3D case to confirm this. The matrix $\boldsymbol{E}$ is given as [34]

$$\boldsymbol{E} = \begin{bmatrix} \dfrac{E}{1-\upsilon^2} & \dfrac{\upsilon E}{1-\upsilon^2} & 0 \\ \dfrac{\upsilon E}{1-\upsilon^2} & \dfrac{E}{1-\upsilon^2} & 0 \\ 0 & 0 & \dfrac{E}{2(1+\upsilon)} \end{bmatrix}, \tag{4}$$

where E is the Young's modulus and υ is Poisson's ratio.

For the mass matrix $\boldsymbol{M}$, we consider a diagonal lumped mass matrix [36] of the form

$$\boldsymbol{M} = \begin{bmatrix} m_1 & & \\ & \ddots & \\ & & m_N \end{bmatrix}, \tag{5}$$

which is purely diagonal and where m_i corresponds to the element region (area in 2D, volume in 3D) multiplied by the density.

For the damping matrix, we assume mass proportional damping (this is equivalent to Rayleigh damping [37] with the appropriate choice of constants) of the form

$$\boldsymbol{C} = \alpha \boldsymbol{M}. \tag{6}$$

Using the diagonal forms of the mass and damping matrices has the computational advantages of being easy to compute, store and invert.

For the time derivative, we use the central finite difference method [38] to arrive at

$$\boldsymbol{M}\frac{\boldsymbol{u}_{t+1} - 2\boldsymbol{u}_t + \boldsymbol{u}_{t-1}}{\delta t^2} + \boldsymbol{C}\frac{\boldsymbol{u}_{t+1} - \boldsymbol{u}_{t-1}}{2\delta t} + \boldsymbol{K}\boldsymbol{u}_t = \boldsymbol{f}, \tag{7}$$

which has an error of $\mathcal{O}(\delta t^2)$. The terms $\boldsymbol{u}_{t-1}$, $\boldsymbol{u}_t$ and $\boldsymbol{u}_{t+1}$ are the displacement vector values at the previous, current and next time steps. By re-arranging equation (7) we arrive at

$$\left(\boldsymbol{M}\frac{1}{\delta t^2} + \boldsymbol{C}\frac{1}{2\delta t}\right)\boldsymbol{u}_{t+1} = \boldsymbol{f} + \left(\boldsymbol{M}\frac{2}{\delta t^2} - \boldsymbol{K}\right)\boldsymbol{u}_t + \left(\boldsymbol{C}\frac{1}{2\delta t} - \boldsymbol{M}\frac{1}{\delta t^2}\right)\boldsymbol{u}_{t-1}. \tag{8}$$

Due to the choice of the diagonal damping matrix $\boldsymbol{C}$ and the diagonal mass matrix $\boldsymbol{M}$, the expression $\left(\boldsymbol{M}\frac{1}{\delta t^2} + \boldsymbol{C}\frac{1}{2\delta t}\right)$ that appears in equation (8) can easily be inverted. The matrices $\boldsymbol{K}, \boldsymbol{M}, \boldsymbol{C}$ and vector $\boldsymbol{f}$ can be calculated and stored before the time-marching begins and do not need to be recomputed at each time step.

2.1.2. Finite element formulation for fluid materials

We proceed with deriving the finite element matrices for fluid materials. We do this directly from the constitutive equation for a compressible fluid. The constitutive equation for a compressible Stokesian fluid with Newtonian viscosity alongside a full derivation can be found in [3]. Although the full derivation is out of scope for this paper, some necessary equations and their context are provided in what follows. The constitutive equation for a compressible fluid is given as [3]

$$\sigma_{ij} = -p\delta_{ij} - \frac{2}{3}\dot{\mu}\dot{\epsilon}_{kk}\delta_{ij} + 2\dot{\mu}\dot{\epsilon}_{ij}, \tag{9}$$

where σ_{ij} is the stress tensor, p is the equilibrium pressure, $\dot{\mu}$ is the dynamic viscosity of the fluid, $\dot{\epsilon}$ is the strain rate and δ_{ij} the Kronecker delta. It follows that ϵ is the strain. Considering the static part of the equation we arrive at

$$\sigma_{xx} = \sigma_{yy} = \sigma_{zz} = -p = \lambda(\epsilon_{xx} + \epsilon_{yy} + \epsilon_{zz}). \tag{10}$$

Here, λ is the bulk modulus of the fluid, which is related to the acoustic speed of the fluid, c, and its density, ρ, as

$$\lambda = \rho c^2. \tag{11}$$

Thus, without loss of generality, over a 2-dimensional $x - y$ plane, the stress-strain and stress-strain rate relationships in matrix form are

$$\begin{bmatrix} \sigma_{xx} \\ \sigma_{yy} \\ \sigma_{xy} \end{bmatrix} = \begin{bmatrix} \lambda & \lambda & 0 \\ \lambda & \lambda & 0 \\ 0 & 0 & 0 \end{bmatrix} \begin{bmatrix} \epsilon_{xx} \\ \epsilon_{yy} \\ \epsilon_{xy} \end{bmatrix} + \begin{bmatrix} -\frac{4}{3}\dot{\mu} & \frac{2}{3}\dot{\mu} & 0 \\ \frac{2}{3}\dot{\mu} & -\frac{4}{3}\dot{\mu} & 0 \\ 0 & 0 & -\mu \end{bmatrix} \begin{bmatrix} \dot{\epsilon}_{xx} \\ \dot{\epsilon}_{yy} \\ \dot{\epsilon}_{xy} \end{bmatrix}. \tag{12}$$

The matrices defined in Equation (12) are then used to calculate $\boldsymbol{D}$ and $\dot{\boldsymbol{D}}$ and which are needed in the stiffness and element damping matrices used in the finite element assembly for the fluid material. These are

$$\boldsymbol{D} = \begin{bmatrix} \lambda & \lambda & 0 \\ \lambda & \lambda & 0 \\ 0 & 0 & 0 \end{bmatrix}, \quad \dot{\boldsymbol{D}} = \begin{bmatrix} -\frac{4}{3}\dot{\mu} & \frac{2}{3}\dot{\mu} & 0 \\ \frac{2}{3}\dot{\mu} & -\frac{4}{3}\dot{\mu} & 0 \\ 0 & 0 & -\dot{\mu} \end{bmatrix}. \tag{13}$$

For inviscid fluids, where we only want to damp out the shear motion, we can use a simplified version of the matrix $\dot{D}$, by setting all entries to 0, apart from the value at position $\dot{D}_{3,3}$. The damping coefficient should be set as small as possible to aid with numerical efficiency. The local element stiffness and local element damping matrices can then be assembled (in parallel, without needing to recalculate the matrix $\boldsymbol{B}$ for both $\boldsymbol{K}$ and $\boldsymbol{C}$) as follows

$$\boldsymbol{K}^e = \boldsymbol{B}^T \boldsymbol{D} \boldsymbol{B}, \tag{14}$$

$$\boldsymbol{C}^e = \boldsymbol{B}^T \dot{\boldsymbol{D}} \boldsymbol{B}. \tag{15}$$

The mass matrix retains its form from the solid case, i.e. proportional to element mass on the diagonal. Matrix $\boldsymbol{B}$ in Equation (14) is the strain-displacement matrix introduced in Equation (3). These are well-known in the literature [35] and depend on the choice of element and the numerical quadrature scheme. We show the formulation for the under-integrated or reduced integration quadrilateral element, i.e. the element with one point of integration in the centre. This has been demonstrated in [25] to reduce, alongside irrotational constraints or damping, spurious modes which are a particular issue for displacement-based fluid formulation [39]. For a quadrilateral with diagonal nodes at points $[-1,-1]$ and $[1,1]$ with shape functions

$$\boldsymbol{N}^e = \frac{1}{4}\begin{bmatrix} (1+x)(1-y) \\ (1-x)(1-y) \\ (1+x)(1+y) \\ (1-x)(1+y) \end{bmatrix}, \tag{16}$$

the strain-displacement matrix $\boldsymbol{B}$ is given as

$$\boldsymbol{B} = \begin{bmatrix} \frac{\partial \boldsymbol{N}^e_1}{\partial x} & 0 & \frac{\partial \boldsymbol{N}^e_2}{\partial x} & 0 & \frac{\partial \boldsymbol{N}^e_3}{\partial x} & 0 & \frac{\partial \boldsymbol{N}^e_4}{\partial x} & 0 \\ 0 & \frac{\partial \boldsymbol{N}^e_1}{\partial y} & 0 & \frac{\partial \boldsymbol{N}^e_2}{\partial y} & 0 & \frac{\partial \boldsymbol{N}^e_3}{\partial y} & 0 & \frac{\partial \boldsymbol{N}^e_4}{\partial y} \\ \frac{\partial \boldsymbol{N}^e_1}{\partial y} & \frac{\partial \boldsymbol{N}^e_1}{\partial x} & \frac{\partial \boldsymbol{N}^e_2}{\partial y} & \frac{\partial \boldsymbol{N}^e_2}{\partial x} & \frac{\partial \boldsymbol{N}^e_3}{\partial y} & \frac{\partial \boldsymbol{N}^e_3}{\partial x} & \frac{\partial \boldsymbol{N}^e_4}{\partial y} & \frac{\partial \boldsymbol{N}^e_4}{\partial x} \end{bmatrix}. \tag{17}$$

If we consider the single integration point to be from the first order Gaussian quadrature scheme [40] which is commonly used for bilinear quadrilateral elements with reduced integration, at point $[0,0]$ we have

$$\boldsymbol{B} = \frac{1}{4}\begin{bmatrix} -1 & 0 & 1 & 0 & 1 & 0 & -1 & 0 \\ 0 & -1 & 0 & -1 & 0 & 1 & 0 & 1 \\ -1 & -1 & -1 & 1 & 1 & 1 & 1 & -1 \end{bmatrix}. \tag{18}$$

Having derived the formulae for assembling the necessary matrices, we now recall the spatial FE formulation from Equation (1) and its finite difference in time formulation from Equation (8). One challenging step becomes immediately apparent - Equation (8) requires inverting $\left(\boldsymbol{M}\frac{1}{\delta t^2} + \boldsymbol{C}\frac{1}{2\delta t}\right)$. It is no longer possible to execute this efficiently owing to the non-diagonal structure of the damping matrix $\boldsymbol{C}$ used for the fluid elements. Since the GPU FE method works best for explicit time domain methods [41], a new approach must be developed. We thus propose and implement the following novel modification of the central finite difference scheme:

$$\boldsymbol{M}\frac{\boldsymbol{u}_{t+1} - 2\boldsymbol{u}_t + \boldsymbol{u}_{t-1}}{\delta t^2} + \boldsymbol{C}\frac{\boldsymbol{u}_t - \boldsymbol{u}_{t-1}}{\delta t} + \boldsymbol{K}\boldsymbol{u}_t = \boldsymbol{f}. \tag{19}$$

The difference in Equation (19) compared to Equation (7) and thus other numerical formulations found in the literature such as [25,39] is that the first order time derivative multiplied by $\boldsymbol{C}$ is changed to depend purely on values at $\boldsymbol{u}_t$ and $\boldsymbol{u}_{t-1}$ which are known. Thus $\boldsymbol{u}_{t+1}$ can be rearranged to

$$\boldsymbol{u}_{t+1} = \delta t^2 \boldsymbol{M}^{-1}(\boldsymbol{f} - \boldsymbol{K}\boldsymbol{u}_t) + 2\boldsymbol{u}_t - \boldsymbol{u}_{t-1} + \delta t \boldsymbol{M}^{-1}\boldsymbol{C}(\boldsymbol{u}_{t-1} - \boldsymbol{u}_t). \tag{20}$$

As in [10], we can compute this as

$$\boldsymbol{u}_{t+1} = \boldsymbol{f}' + \boldsymbol{C}'\boldsymbol{u}_{t-1} + \boldsymbol{K}'\boldsymbol{u}_t, \tag{21}$$

where we have introduced the modified matrices

$$\boldsymbol{K}' = -\delta t^2 \boldsymbol{M}^{-1}\boldsymbol{K} + 2\boldsymbol{I} - \delta t \boldsymbol{M}^{-1}\boldsymbol{C}, \tag{22}$$

$$\boldsymbol{C}' = -\boldsymbol{I} + \delta t \boldsymbol{M}^{-1}\boldsymbol{C}, \tag{23}$$

and the vector

$$\boldsymbol{f}' = \delta t^2 \boldsymbol{M}^{-1}\boldsymbol{f}. \tag{24}$$

Now, as in [10], $\boldsymbol{K}'$ and $\boldsymbol{C}'$ remain constant and $\boldsymbol{f}'$ can be precomputed as it does not change based on the time-stepping during the simulation. Hence they can be assembled, stored and used for all time steps. The modified numerical scheme we have introduced and described above in Equation (19) has the advantage that it is explicit in time, without relying on inversion of the matrix $\boldsymbol{C}$, and is better suited for GPU calculations. The stability of the method remains the same as it occupies the same stencil in time [42], requiring the same number of nodal points. Thus, it has the same Courant-Friedrichs-Lewy condition [38] as the standard central difference scheme i.e.

$$c\frac{\Delta t}{\Delta x} < 1. \tag{25}$$

The numerical error of this method for the calculation of the acceleration is $\mathcal{O}(\delta t^2)$. The error of this method related to the modified numerical calculation of the velocity increases from $\mathcal{O}(\delta t^2)$ to $\mathcal{O}(\delta t)$ due to the use of the current time step instead of the future one. As the total error of this method is bounded by the highest error present, the total error is $\mathcal{O}(\delta t)$, implying we will need higher refinement than the conventional finite difference method to achieve the same accuracy. We note that higher order implies lower error in numerical methods.

To summarise, we have introduced and derived a finite element formulation for fluid materials which damps out the shearing motion through the use of a non-diagonal damping matrix alongside the use of a reduced-integration Gaussian quadrature scheme and is displacement based. It is thus compatible with existing software designed for solid materials and explicit in time and suitable for GPU calculations.

3. Computational performance of the method

Direct timing comparisons between the formulation and implementation of the method on a GPU described in this paper and existing finite element (FE) software for fluid-solid interaction are not straightforward, hence, they are not presented in this paper. The primary reason for this is the significant differences in speed, memory, and cost characteristics between GPUs and CPUs. Consequently, we cannot provide directly comparable results between a GPU and a CPU implementation that would fairly represent the advantages and disadvantages of this method. FE software packages are also often heavily dependent on not just the formulation used. The choice of programming language and compiler optimisations [43] also significantly impact the performance of the algorithms. Furthermore, there is frequent improvement in all aspects of computational mathematics [44] and hardware, which can complicate direct timing comparisons. The formulation in this paper and others found in the literature will benefit from such computational improvements.

Despite the above, it is appreciated that timing comparisons can help validate the proposed performance improvements claimed by this method. Therefore, as we know the timing ratio of Pogo Solid to conventional CPU-based FE software, if we calculate the ratio of the fluid-solid implementation to the solid implementation in Pogo (the method presented and implemented in this paper), we can compare the GPU-based method presented in this paper to CPU-based methods via the method described below. A mathematical description of this can be as follows,

$$\frac{\text{Pogo Fluid-Solid GPU}}{\text{Conventional CPU}} = \frac{\text{Pogo Fluid-Solid GPU}}{\text{Pogo Solid GPU}} \times \frac{\text{Pogo Solid GPU}}{\text{Conventional CPU}}. \tag{26}$$

This way of calculating the performance difference also has the benefit of being run on the same underlying hardware for a more accurate comparison.

We setup a pair of simulations as follows: We define a square grid of rectangular elements. For the first simulation, this is fully solid and for the second simulation we set the right-half to be fluid. We progressively increase the size of the square grid to obtain measurements across a wide-range of total number of degrees of freedom. We run the sim-

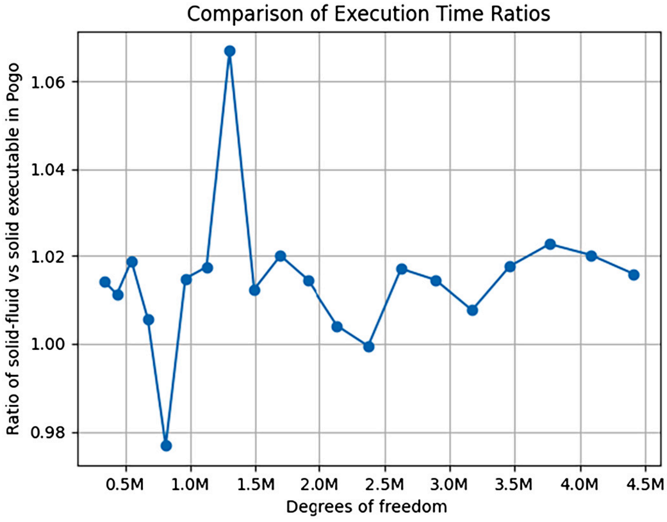

Fig. 1. Ratio of solid-fluid vs fluid executable in Pogo.

ulation at grid size three times and take the average, to mitigate any anomalous results inherent in timing computing processes.

The results of the two measurements are depicted in Fig. 1, where the ratio of Pogo-Fluid-Solid to Pogo-Solid is plotted. A marginal slowdown of approximately 2% is observed when comparing the solid-fluid executable to the solid executable, even though some deviations appear even when averaging. Despite the extra computation required by the method presented in this paper, it does not significantly increase the slowdown compared to the GPU FE method for solid materials introduced in [10]. This method has proven to be more efficient than similar CPU-based methods. Running GPU FE software has been demonstrated to offer significant improvements, even when accounting for the change in hardware, and the author refers the reader to such implementations for further reference [10]. For the examples that follow, we use the method described in this paper, implemented in Pogo [10], although the proposed method is sufficiently generic to be implemented in any other FE software.

4. Numerical results

In this section, we verify the theoretical fluid formulation proposed in Section 2.1.2 with numerical simulations. We compare our results with those of known methods and previously published results. These are scattering patterns from Faran for solid cylinders [11], Doolittle for solid annuli [45] and Tamarkin for fluid inclusions [46]. We also compare against velocity, attenuation and existence of guided-wave wave modes from a commercially-available software Disperse [3]. Of particular importance to the validation is capturing the Scholte-wave [14], which propagates along the interface of an elastic solid and an ideal fluid, using our formulation. We have chosen these use cases as they capture a wide range of properties of the fluid and solid and represent physical scenarios which are of interest to both practitioners and researchers. Furthermore, they allow us to test all properties of the wave equation simulated, both at low frequencies, of interest to the underwater acoustic community and high frequencies, of interest to the NDT community. We initially show results for inviscid fluids, although we believe this method will generalise well to viscous fluid also, as our derivation in Section 2.1.2 allows us to incorporate viscous damping, by using the full version of matrix $\dot{\boldsymbol{D}}$ given in Equation (13), this needs to be properly validated.

The damping parameter to handle hourglassing is set to 0.05%, although no full analytical solution has been found for the efficient choosing of this parameter. We have also observed for very high refinements that the damping parameter is not necessary (i.e. can be set to zero) although this increases the computational requirements of the problem.

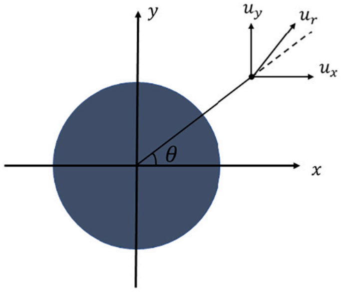

Fig. 2. Radial displacement.

It's also worth noting that excessively high damping parameters can lead to the degradation of the solution. In practice, it is recommended to conduct convergence testing using a simple problem with a known analytical solution. Once an accurate solution is achieved, the same damping parameter can be applied to more complex problems. Additionally, visual inspection of the field can help to spot any immediate problems in the deterioration of the solution, which assuming the necessary refinement, indicates hourglassing issues. An analytical solution to the damping parameter is a good avenue for further research. All the simulations presented in this paper have further relied on the (elastic) orthogonal hourglass control method described in [24] which relies on using an additional artificial stiffness to reduce this phenomenon.

4.1. *Scattering from cylindrical structures*

We now proceed to compute and compare scattering results across three separate related physical cases of underwater objects. We define the radial displacement as

$$\boldsymbol{u}_r = \boldsymbol{u}_x \cos\theta + \boldsymbol{u}_y \sin\theta, \tag{27}$$

and our results in Section 4.1 will be given in radial displacement. To achieve scattered results numerically, we use the following relation

$$\boldsymbol{u}_r^{tot} = \boldsymbol{u}_r^{inc} + \boldsymbol{u}_r^{scatt}, \tag{28}$$

where $\boldsymbol{u}_r^{tot}$ is the total displacement, $\boldsymbol{u}_r^{inc}$ is the displacement of a homogeneous field (i.e. no scatterer) and $\boldsymbol{u}_r^{scatt}$ is the scattered displacement. We compute two FE simulations, one with the scatterer, and one with a homogeneous field, giving us $\boldsymbol{u}_r^{tot}$ and $\boldsymbol{u}_r^{inc}$, allowing us to calculate $\boldsymbol{u}_r^{scatt}$ as

$$\boldsymbol{u}_r^{scatt} = \boldsymbol{u}_r^{tot} - \boldsymbol{u}_r^{inc}. \tag{29}$$

As we are in a displacement-based setting, the responses for the displacements $\boldsymbol{u}_x$ and $\boldsymbol{u}_y$ are readily available. An illustration of this can be found in Fig. 2.

In all simulations in Section 4.1, the excited plane wave travels from the right and we place response nodes at a distance which is given below for each scatterer, from the centre of the scatterer. For the simulation in Section 4.1.1 these are at a distance of 2.5 m and for the simulations in Section 4.1.2 these are at a distance of 10 m. We have 360 of these at the measurement radius, spaced apart by 1°, covering the range of $0° - 359°$. Due to the nature of the FE method, we can either compute the response in the far field (arbitrary distances can be measured given appropriate computational power and storage) or these can be calculated straightforwardly from the near field results. In all cases, we use a Courant-Friedrichs-Lewy [38] number of 0.8 with respect to the highest velocity in the simulation (usually the solid longitudinal wave speed) to determine the time step

$$\mathrm{d}t = \frac{\mathrm{d}x}{c_L} \times \mathrm{Courant} \tag{30}$$

and we allow enough time for the wave to pass across the domain and back with reference to the fluid wave speed. We process the time-

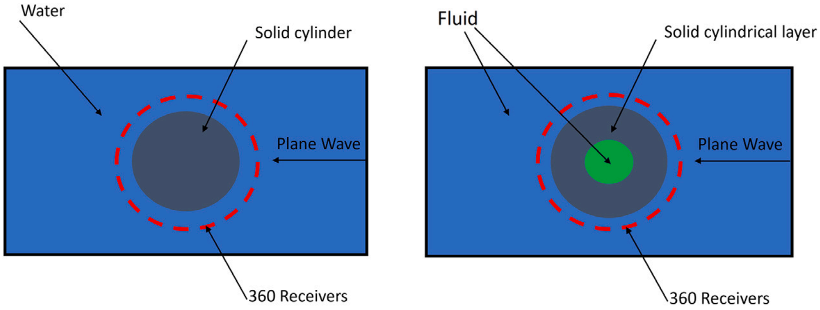

(a) Solid cylinder

(b) Cylindrical layered media (annulus)

Fig. 3. A schematic showing a (a) solid cylinder and (b) annulus in water insonified by a plane wave, the red dashed lines show the receiver points.

Table 1
Material properties used in numerical examples.

Material	Longitudinal wave speed (m/s)	Shear wave speed (m/s)	Density (kg/m^3)
Steel	5960	3260	7932
Perspex	2730	1430	1180
Water	1500	-	1000
Air	350	-	1.125
Glycerine	1860	-	1258

domain signals from our FE method using an FFT and extract a discrete frequency (closest to the excitation frequency) to compare with the analytical solution in the frequency domain. For a quantitative comparison, we calculate the relative error norm defined as

$$\frac{||\boldsymbol{u}_{true} - \boldsymbol{u}_{FE}||_1}{||\boldsymbol{u}_{true}||_1} \tag{31}$$

of our measured FE scattering in the frequency domain as detailed above, versus the analytical solution, where $||\boldsymbol{u}||_1$ is the ℓ_1 vector norm of $\boldsymbol{u}$.

The analytical expression for the scattered pressure field in infinitely long cylindrical structures in inviscid fluids can be found in [45], and is given for a single frequency as

$$p_r^{scatt}(r,\theta) = \sum_{n=0}^{\infty} i^n \epsilon_n b_n H_n^{(1)}(k_{ext} r) \cos n\theta, \tag{32}$$

and from this, we can calculate the radial derivative to give us the scattered displacement as

$$u_r^{scatt}(r,\theta) = \sum_{n=0}^{\infty} i^n \epsilon_n b_n k_{ext} H_n'^{(1)}(k_{ext} r) \cos n\theta, \tag{33}$$

where ϵ_n is the Neumann factor defined as $\epsilon_0 = 1$, $\epsilon_n = 2$, for $n > 0$, b_n are the coefficients which define the scattered fields for each scatterer which must be evaluated in each case and are well-known in the literature, $H_n^{(1)}$, $H_n'^{(1)}$ are Hankel functions of the first kind and their respective derivatives, k_{ext} is the radial wavenumber in the exterior inviscid fluid, r is the distance from the centre of the cylindrical scatterer and θ is the angular position.

4.1.1. Solid cylinder

The analytical expression for the radial displacement in a solid-fluid scattering problem for an infinitely long solid cylinder submerged in fluid can be found in [11] but can also be calculated from Equation (33) with b_n given as

$$b_n = \frac{1}{D} \begin{vmatrix} \beta_1 & \alpha_{12} & \alpha_{14} \\ \beta_2 & \alpha_{22} & \alpha_{24} \\ 0 & \alpha_{32} & \alpha_{34} \end{vmatrix}, \tag{34}$$

where D is

$$D = \begin{vmatrix} \alpha_{11} & \alpha_{12} & \alpha_{14} \\ \alpha_{21} & \alpha_{22} & \alpha_{24} \\ 0 & \alpha_{32} & \alpha_{34} \end{vmatrix}. \tag{35}$$

We have used $|A|$ to represent the determinant of the matrix A. Full details of the coefficients α_{ij}, b_i found in Equations (34)-(35) can be found in [45]. The considered setup of this is schematically depicted in Fig. 3a. The domain is -10 m $< x <$ 10 m, -10 m $< y <$ 10 m with a grid spacing of 12.5 mm corresponding to 1601×1601 grid points. Our forcing vector is a three-cycle Hann-windowed toneburst. The frequencies investigated ranged from 200 Hz to 1 kHz. We placed absorbing layers [47] on the boundaries of the numerical model to satisfy the Sommerfeld radiation condition [48], as we are representing an infinite continuous space using a finite discrete space in our numerical method.

We consider different materials for the solid, such as steel and perspex, whose parameters can be found in Table 1, to demonstrate capabilities in low and high impedance situations. Furthermore, perspex has the interesting property that it has a shear wave speed less than the acoustic wavespeed of the surrounding fluid, confirming the accuracy of the model in different use-cases.

We first consider scattering from a steel cylinder for $k_{ext}a$ between 0.84 and 4.19. Here a is the radius of the scatterer. These correspond to frequencies ranging from 200 Hz to 1000 Hz with a fixed radius of 1 m. In the simulations, we fixed the radius and modified the frequency, so we can keep the geometry fixed and eliminate the need for remeshing.

The results are shown in Fig. 4. There is good agreement throughout the considered range, with the exception of scattered angles perpendicular to the propagation direction, which show some deviation. This can be attributed to low plane wave transmission at grazing incidence and a greater effect of structured mesh staircasing, which might be improved by the use of a conforming mesh, although this does introduce additional complexities during pre-processing as we must carefully define the object boundaries, the sources and receivers and accurately mesh around these. In [49], it is shown that both approaches are equally good for waves in polycrystals, which suffer from the same error regarding staircasing, and thus structured grids are normally used due to the comparative ease of use. The relative errors or the scattering field at the frequencies shown computed with Equation (31) are 1.05%, 1.03%, 1.51%, and 2.17% respectively. At a lower mesh refinement (25 mm), the errors increased to 1.12%, 1.16%, 2.68%, and 4.37% respectively. This clearly shows a reduction in error as we use a finer mesh, and therefore the convergence of the method. It should be noted that there will always be a trade-off in the additional computational power and storage required to run calculations on a finer mesh for higher accuracy, and it is left to the reader to decide what error-rate is suitable for their simulations. The discrepancy at higher frequencies is to be expected as we have comparatively less resolution per wavelength compared to lower frequencies, as we kept the element sizes fixed for each set of simulations.

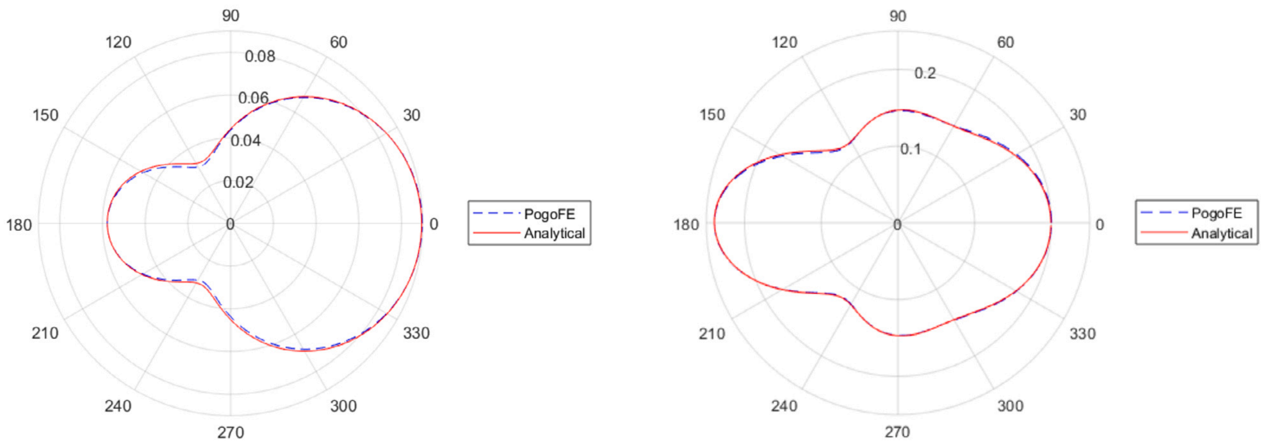

(a) Scattering at 200 Hz

(b) Scattering at 250 Hz

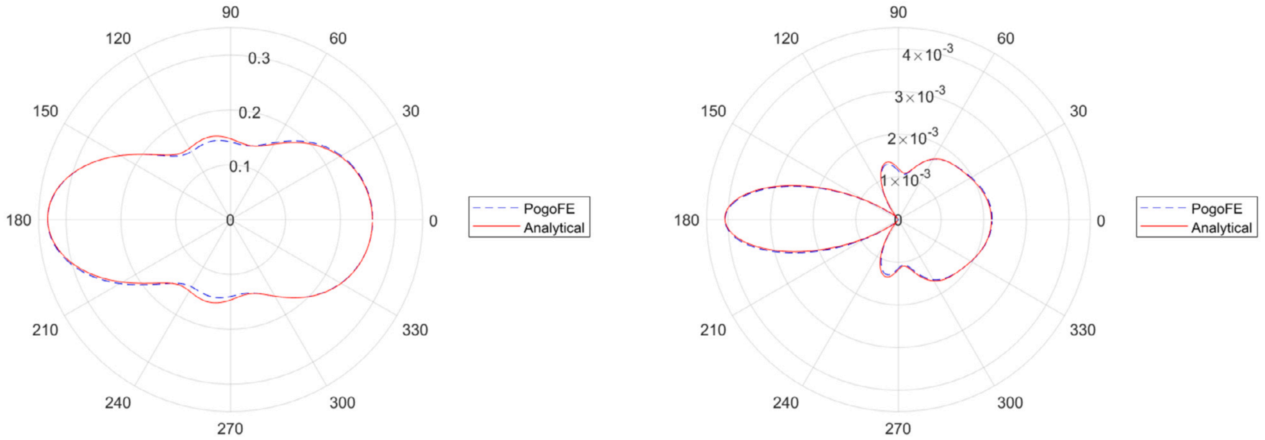

(c) Scattering at 500 Hz

(d) Scattering at 1 kHz

Fig. 4. Scattering results for steel cylinder submerged in water compared to analytical results. Plane wave travelling from right to left.

We repeat the simulations for a perspex cylinder. The geometrical setup remains the same as described above, and we use a central frequency of 1 kHz with a cylinder radius of 1 m. Results for this can be found in Fig. 5 with the equivalent-sized steel cylinder present for comparison. This has a relative error of 3.36% for the same mesh discretisation as the steel cylinder. While this may appear initially surprising, the explanation for this is two-fold. Perspex has a lower longitudinal and shear wavespeed than steel, and thus needs further refinement to maintain the same number of elements per wavelength. Furthermore, as we can see in Fig. 6, the perspex scattering pattern is much more susceptible to small changes in frequency compared to the steel pattern. For a ±1% shift in frequency at 1 kHz, the relative error of the analytical solution of the steel cylinder scattering is 1.3% (both downwards and upwards), whereas for a ±1% shift in frequency at 1 kHz, the relative error of the analytical solution of the perspex cylinder scattering is 3.26% for the downward shift and 4.20% for the upward shift, indicating that errors are not linear in frequency change.

4.1.2. Layered cylindrical media

For the second scattering example, we consider solid cylindrically layered media submerged in fluid and enclosing another fluid. Analytical results for this case can be calculated from Equation (33) with b_n given as

$$b_n = \frac{1}{D}\begin{vmatrix} \beta_1 & \alpha_{12} & \alpha_{13} & \alpha_{14} & \alpha_{15} & 0 \\ \beta_2 & \alpha_{22} & \alpha_{23} & \alpha_{24} & \alpha_{25} & 0 \\ 0 & \alpha_{32} & \alpha_{33} & \alpha_{34} & \alpha_{35} & 0 \\ 0 & \alpha_{42} & \alpha_{43} & \alpha_{44} & \alpha_{45} & \alpha_{46} \\ 0 & \alpha_{52} & \alpha_{53} & \alpha_{54} & \alpha_{55} & \alpha_{56} \\ 0 & \alpha_{62} & \alpha_{63} & \alpha_{64} & \alpha_{65} & 0 \end{vmatrix}, \tag{36}$$

where D is given by

$$D = \begin{vmatrix} \alpha_{11} & \alpha_{12} & \alpha_{13} & \alpha_{14} & \alpha_{15} & 0 \\ \alpha_{21} & \alpha_{22} & \alpha_{23} & \alpha_{24} & \alpha_{25} & 0 \\ 0 & \alpha_{32} & \alpha_{33} & \alpha_{34} & \alpha_{35} & 0 \\ 0 & \alpha_{42} & \alpha_{43} & \alpha_{44} & \alpha_{45} & \alpha_{46} \\ 0 & \alpha_{52} & \alpha_{53} & \alpha_{54} & \alpha_{55} & \alpha_{56} \\ 0 & \alpha_{62} & \alpha_{63} & \alpha_{64} & \alpha_{65} & 0 \end{vmatrix}, \tag{37}$$

and for full details of the coefficients α_{ij}, β_i found in Equations (36)-(37) see [45].

A schematical diagram of the setup can be found in Fig. 3b. We consider the same solid materials as those in Section 4.1.1 to demonstrate capabilities in low and high impedance situations. The exterior and interior layers are of fluid, not necessarily of the same material, which surround a solid layer. The interior fluid layer and solid layer both have a radius of 1 m for a total radius of 2 m. The domain is -40 m $< x <$ 40 m, -40 m $< y <$ 40 m with a grid spacing of 50 mm corresponding to 1601 × 1601 grid points. The forcing vector was a three-cycle

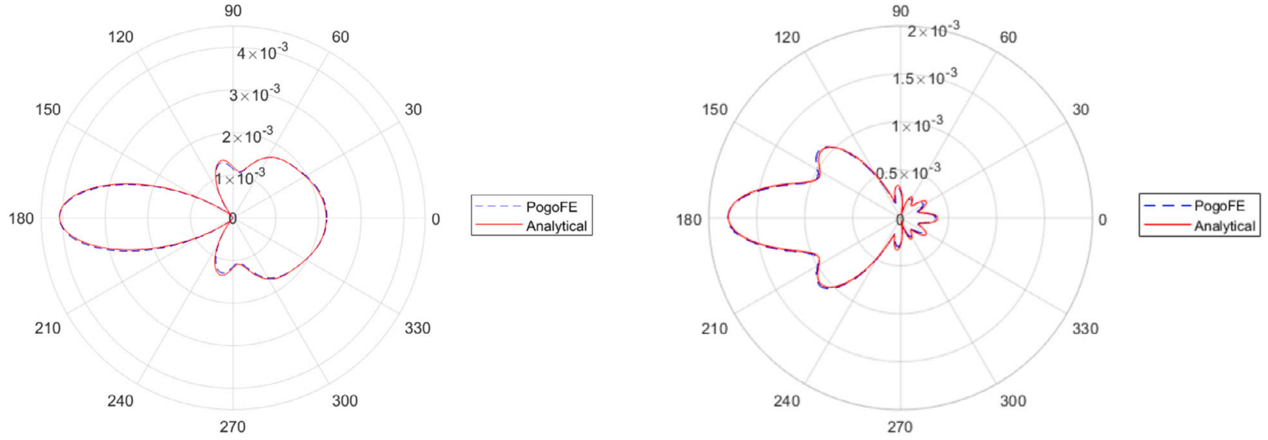

(a) Steel cylinder

(b) Perspex cylinder

Fig. 5. Scattering patterns from (a) steel cylinder and (b) perspex cylinder submerged in water at 1 kHz. Plane wave travelling from right to left.

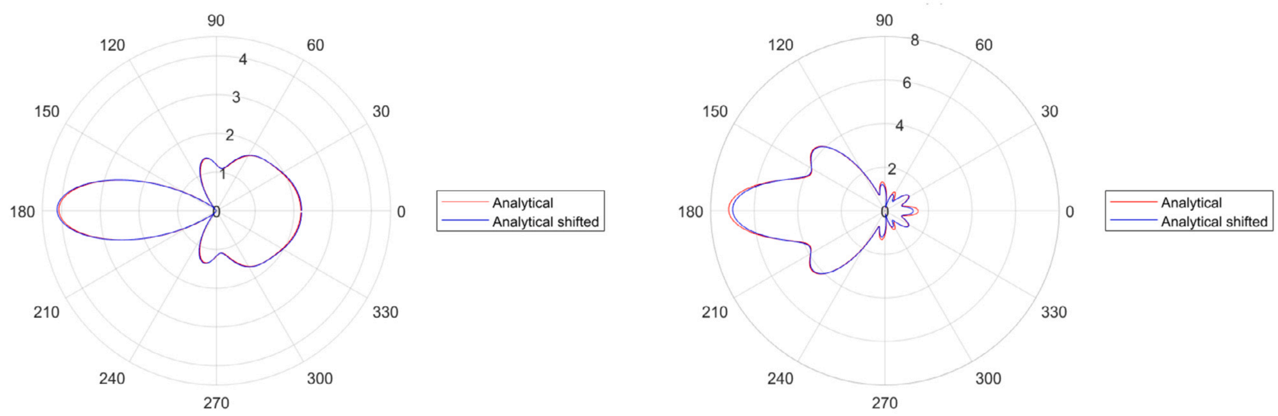

(a) Steel cylinder

(b) Perspex cylinder

Fig. 6. Analytical and frequency-shifted scattering patterns from (a) steel cylinder and (b) perspex cylinder submerged in water at 1 kHz and 0.99 kHz respectively. Plane wave travelling from right to left.

Hann-windowed toneburst with a central frequency of 500 Hz. Absorbing boundaries are also placed on the boundaries of the setup as detailed in Section 4.1.1.

In this configuration, we used steel and perspex for solid layers, water as the exterior fluid and both water and air as the interior layer, giving a total of four computed cases. In Fig. 7, which shows the steel layer, we have very little change in the scattering pattern between the air and water interior layers. This is governed by the high density of the solid material compared to that of the interior fluid, so much of the energy is reflected regardless of the filling material. For the perspex layer, the scattering pattern between the two different materials in the interior layer is clearly different as can be seen in Fig. 8. Good agreement can be observed in all cases when comparing with analytical results from [45], with a relative error norm of 2.68%, 3.00% for the steel layer with water and air interiors respectively and 3.73%, 3.19% for the perspex layer with water and air interiors respectively.

The next set of scattering simulations address ultrasonic scattering from liquid cylindrical obstacles. An experimental investigation of this setup was first performed by Tamarkin in [46]. Analytical results for this case can be calculated from Equation (33) with b_n given as

$$b_n = \frac{\begin{vmatrix} \beta_1 & \alpha_{12} \\ \beta_2 & \alpha_{22} \end{vmatrix}}{\begin{vmatrix} \alpha_{11} & \alpha_{12} \\ \alpha_{21} & \alpha_{22} \end{vmatrix}} \tag{38}$$

and for full details of the coefficients found in Equation (38) see [45]. The considered setup is very similar to that in Fig. 3a, with an exception that the solid cylinder is replaced with a fluid one.

We consider a circular fluid inclusion of radius 2 m. The incident plane wave has a central frequency of 500 Hz and we measure at a distance of 10 m from the centre of the cylindrical inclusion. The geometrical aspect of the domain is identical to that above. The circular inclusion material in this case is glycerine. We are using the velocity and density material parameters for glycerine found in Table 1 and we are treating it as inviscid for the purpose of this study. The glycerine inclusion is then surrounded by an infinite water layer and absorbing layers are also placed on the boundaries of the setup as detailed in Section 4.1.1 so we can computationally solve this.

The comparison with analytical results shows excellent agreement at all angles as seen in Fig. 9. Results for this simulation are expected to be more accurate due to the comparable wavespeeds of both glyc-

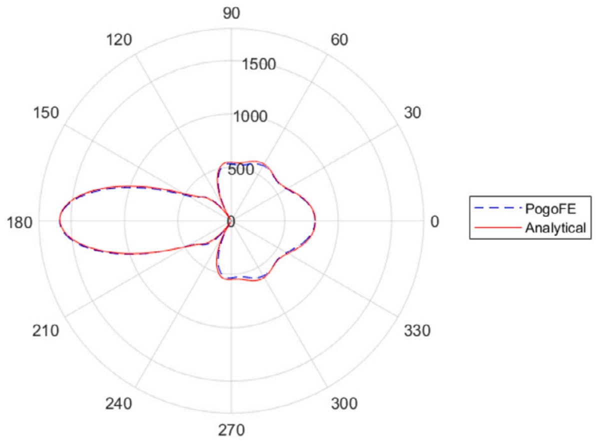

(a) Water interior

(b) Air interior

Fig. 7. Scattering patterns from a steel annulus submerged in water with a (a) water interior and (b) air interior. Plane wave travelling from right to left.

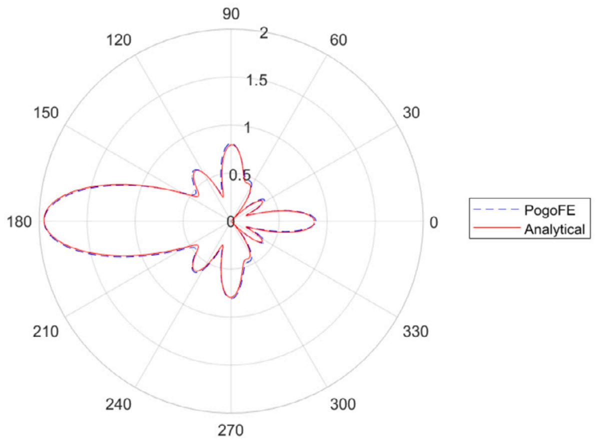

(a) Water interior

(b) Air interior

Fig. 8. Scattering patterns from a perspex annulus submerged in water with a (a) water interior and (b) air interior. Plane wave travelling from right to left.

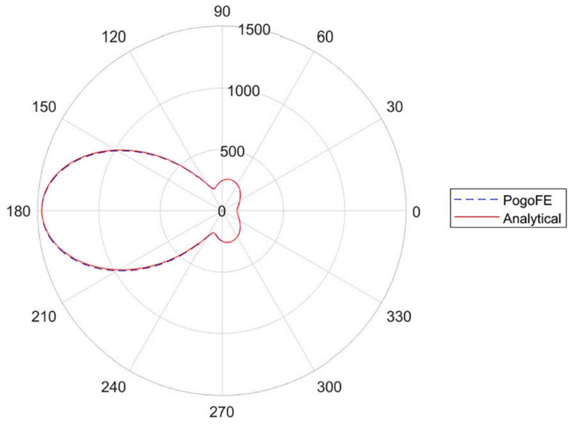

Fig. 9. Scattering pattern for normalised displacement from a cylindrical glycerine inclusion. Plane wave travelling from right to left.

erine and water which allow the Courant-Friedrichs-Lewy number to be closer to 1, as described in [50]. The relative error norm for this example is 1.12%. The fluid inclusion setup addresses the ability to accurately model the interaction between two fluids which is necessary when modelling objects on the sediment interface or buried below it. This computational setup is extremely useful in underwater acoustics. The current state of the art research frequently models the sediment as a fluid, as in [51,52].

4.2. Guided waves in plates

In this section we consider the guided wave context, essential to numerous NDE applications. We investigate three characteristics of guided waves, with further detail given in each corresponding section. These are: the existence of wave modes, phase velocity and attenuation of the A0 mode. The considered setup can be found in Fig. 10. This corresponds to us considering the 2D representation of the cross-section through the solid steel plate, which is 1 mm thick and surrounded by an infinite fluid (water in our case) on either side. The wave propagates in the direction of the plane of the cross-section, left to right in Fig. 10. The domain is 0 mm $< x <$ 150 mm, 0 mm $< y <$ 22 mm with a grid spacing of 0.05 mm corresponding to 3001×441 grid points. We use a Courant number of 0.8 as detailed in Equation (30) and allow for enough time for the wave to travel the domain in the horizontal direction and back. The stiffness reduction method by [47] is once again

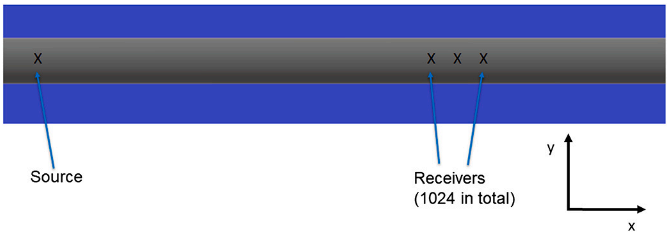

Fig. 10. Schematic of an immersed steel plate alongside cartesian axes.

used and absorbing layers are placed on the vertical boundaries of the setup as detailed in Section 4.1.1. This is to be able to model the infinite fluid in finite space in our finite-element simulations.

4.2.1. *Existence of wavemodes*

A Hann-windowed three-cycled sinusoidal source of 1 MHz excited the 2nd DoF of the node corresponding to the y-direction along the midpoint of the steel plate at $y = 11$ mm. This is expected to excite the antisymmetric modes and not excite the symmetric modes. A series of receivers were placed along the middle of the plate's thickness in the far field. The distance was far enough to allow the wave to propagate and form, so that the guided wave response can be recorded at specific intervals.

To demonstrate the existence of the wave modes, we relied on the two-dimensional Fourier transform method described in [53]. Signal traces are taken from the simulated receivers and converted to the frequency-wavenumber domain using a zero-padded 2D fast Fourier transform.

We then overlaid the result from the 2D fast Fourier transform with theoretical dispersion curves from Disperse [3]. Fig. 11 clearly shows that both A0, A1, A2 and the Scholte wave are captured in the FE solution. The presence of the Scholte wave is particularly encouraging as it is an interface wave, governed by the interaction between the two media at the interface. It also confirms our expectations that our source excitation has excited the antisymmetric modes but not the symmetric ones.

To demonstrate that our model can handle higher frequencies and excite other antisymmetric modes, we repeat the simulation with a central frequency of 5 MHz. We keep the rest of the setup unchanged. Dispersion curves calculated with the 2D fast Fourier transform method (left) are again overlaid with dispersion curves from Disperse (right) and presented in Fig. 12. In this case, we can see that the higher-order A2, A3 and A4 antisymmetric modes are also present.

4.2.2. *Phase velocity*

For the evaluation of the phase velocity, we used a Hann-windowed three-cycled sinusoidal source of 2 MHz applied to the 2nd DoF of the node at the midpoint. We relied on the amplitude spectrum method developed in [54], where we take two signal traces containing the A0 mode in the far field and add them together. We then obtain the amplitude spectrum of the result via a Fourier transform and find the minima from the resulting graph. Phase velocity can be calculated using the following formula

$$c = \frac{2lf}{m}, \tag{39}$$

where c is the guided-wave velocity, l is the distance between the two signals, f is the frequency and m is the index of the minima. The distance between the two response points was 0.01 m. Minima were calculated numerically via Matlab routines and are highlighted on Fig. 13. Fig. 13 also shows the combined signal traces and the FFT of the response. Some ringing and low frequency component is visible in the combined signal traces, but as this is far away from the central frequency it does not affect the results. Due to the nature of the method, the results are given for discrete frequencies, and changing the receiver placement can change these frequencies. In Table 2, we can see that the velocity matches that of Disperse with high accuracy, with relative errors of less than 1%. For the frequency closest to the central frequency, our results are even better, with a near exact match to those calculated using semi-analytical results.

4.2.3. *Attenuation*

Guided waves attenuate due to absorption, scattering and leakage. Absorption and scattering do not contribute to attenuation in this case. We do not have attenuation due to absorption as we are considering an elastic material with no damping, and we have no scattering attenuation as we have no roughness or inhomogeneities in the steel plate.

Leakage in particular occurs in guided waves when the waveguide (in our case the steel plate) is in contact with another medium (the surrounding fluid). The correct prediction of this leakage and therefore the attenuation characteristics are of great importance as they are part of the modal properties of the plate-water system [55].

Modelling attenuation is very sensitive to the contributions of multiple modes present in a signal (it is rarely possible to achieve single mode excitation). Hence, it required careful generation and windowing of signals to achieve accurate results. For excitation, we relied on "mode matching", where the source perfectly matches the displacement and phase characteristics of the desired A0 wave mode. Displacement and phase information for this is readily available from Disperse and can be seen in Fig. 14 and ensures that our simulated wave does not excite any additional modes. We use this information as an input to our forcing vector in our simulations. We then take measurements arbitrarily at two points where we have placed receivers, as can be seen in Fig. 10. In Fig. 15, we can clearly see that the second signal has less amplitude than the first signal, giving a qualitative view of the attenuation. Attenuation is then calculated by computing a Fourier transform of the received signals as shown in Fig. 15, dividing these and we then scale this based on the distance travelled.

The most accurate results for attenuation are achieved around the central frequency of the source. FFT spectra of the signals used in the 1 MHz simulation are shown in Fig. 15. We repeat the attenuation simulation for frequencies of 100 kHz and 200 kHz either side of the original 1 MHz excitation for a total of 5 simulations. In Table 3, we compare the attenuation calculated from FE results to those coming from Disperse. The values computed from the FE simulations agree well with those extracted from Disperse [3], with relative errors of less than 1%. This indicates our fluid formulation can accurately model the leakage phenomenon in guided wave propagation.

5. Conclusions

We derived a novel finite element formulation for modelling ultrasound propagation and scattering in fluid-solid interactions. This uses a displacement-based formulation making it compatible with existing efficient solid FE software suited for solving problems of hundreds of millions of degrees of freedom. A modified finite difference method for the time discretisation has enabled an explicit in-time formulation, without the need of matrix inversion of $\boldsymbol{C}$ necessary for damping out the shearing motion. Due to this explicit in-time formulation, compatibility with explicit time-domain GPU packages such as Pogo is achieved and our formulation is also GPU-accelerated. We have shown validation results for a wide range of use cases, including scattering from solid cylinders, solid cylindrically layered media and fluid inclusions and leaky guided waves scenario. We achieved good agreement with analytical scattering solutions available in the literature. The errors for guided wave phase velocity and attenuation were less than 1%, while capturing the Scholte wave correctly gave us confidence in the implementation of the coupling. For the different cases considered above we consistently get good results for both low frequencies common in underwater acoustics and high frequencies common in NDT settings,

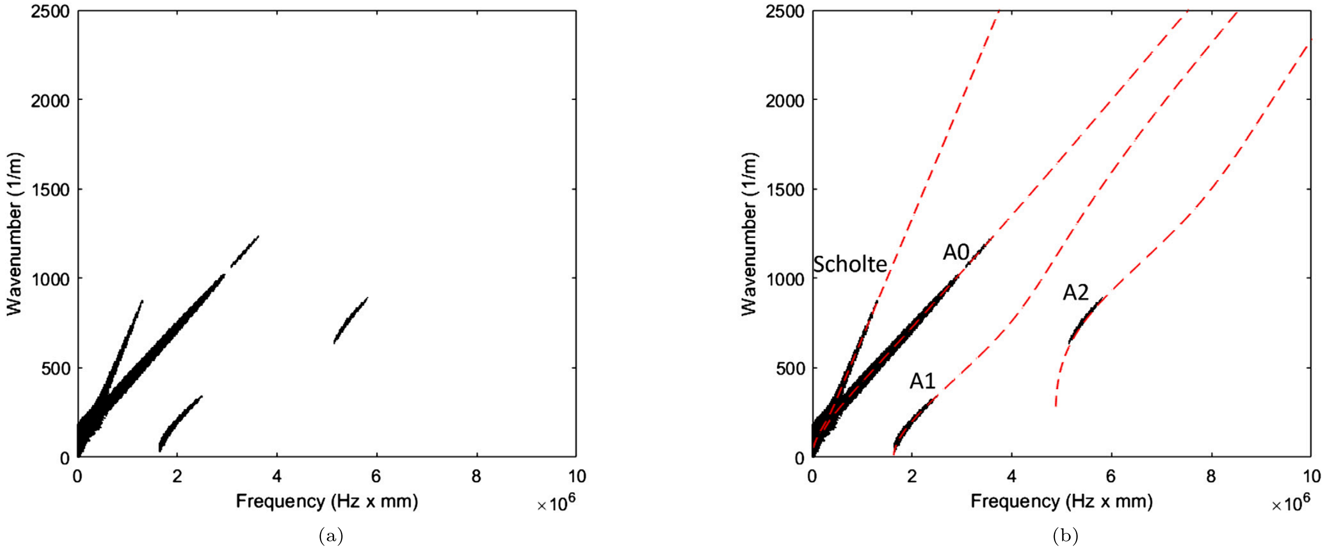

(a)
(b)

Fig. 11. Dispersion curves for a 1 mm thick steel plate submerged in water (a) calculated by processing results from an FE simulation, (b) overlaid with Disperse curves (dotted-lines) at 1 MHz.

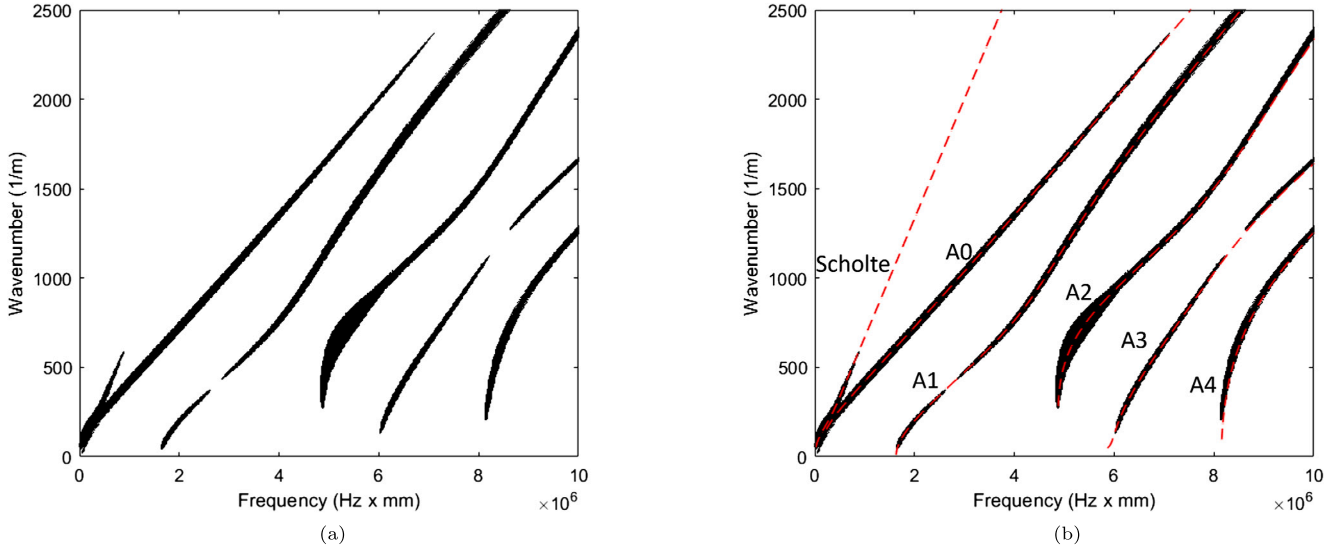

(a)
(b)

Fig. 12. Dispersion curves for a 1 mm thick steel plate submerged in water (a) calculated by processing results from an FE simulation, (b) overlaid with Disperse curves (dotted-lines) at 5 MHz.

Table 2
Comparison of phase velocities between Disperse and FE simulations.

Simulation frequency (MHz)	Disperse frequency (MHz)	Phase velocity from FE (m/ms)	Phase velocity from Disperse (m/ms)	Relative error difference (%)
1.266	1.267	2.532	2.519	0.515
1.589	1.589	2.648	2.643	0.189
1.912	1.912	2.731	2.732	0.0366
2.235	2.235	2.794	2.797	0.108
2.558	2.558	2.842	2.845	0.106

Table 3
Comparison of attenuation between Disperse and FE simulations.

Frequency (kHz)	Attenuation from FE (dB/m)	Attenuation from Disperse (dB/m)	Relative error difference (%)
800	556.1	555.1	0.18
900	530.9	530.7	0.2
1000	511.2	514.2	0.583
1100	498.2	502.6	0.875
1200	496.6	494.6	0.404

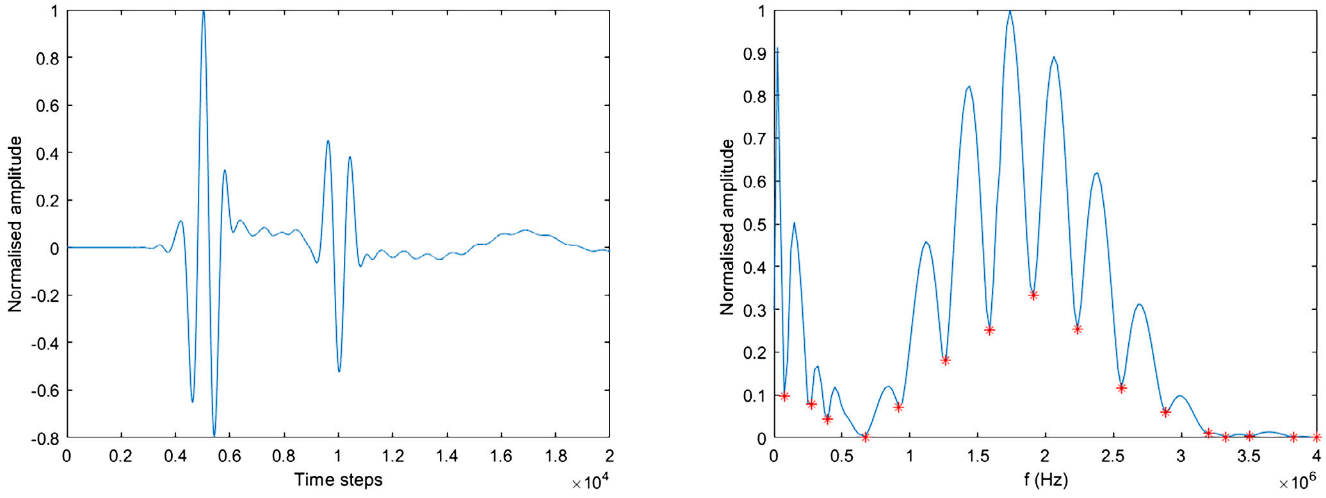

(a) Combined signal traces.

(b) Amplitude spectrum of combined signals.

Fig. 13. (a) Combined signal traces of the A0 propagating wave measured at two points as described in Section 4.2.2 alongside (b) their amplitude spectrum. Red stars in (b) indicated local minima on the graph, found through use of Matlab routines.

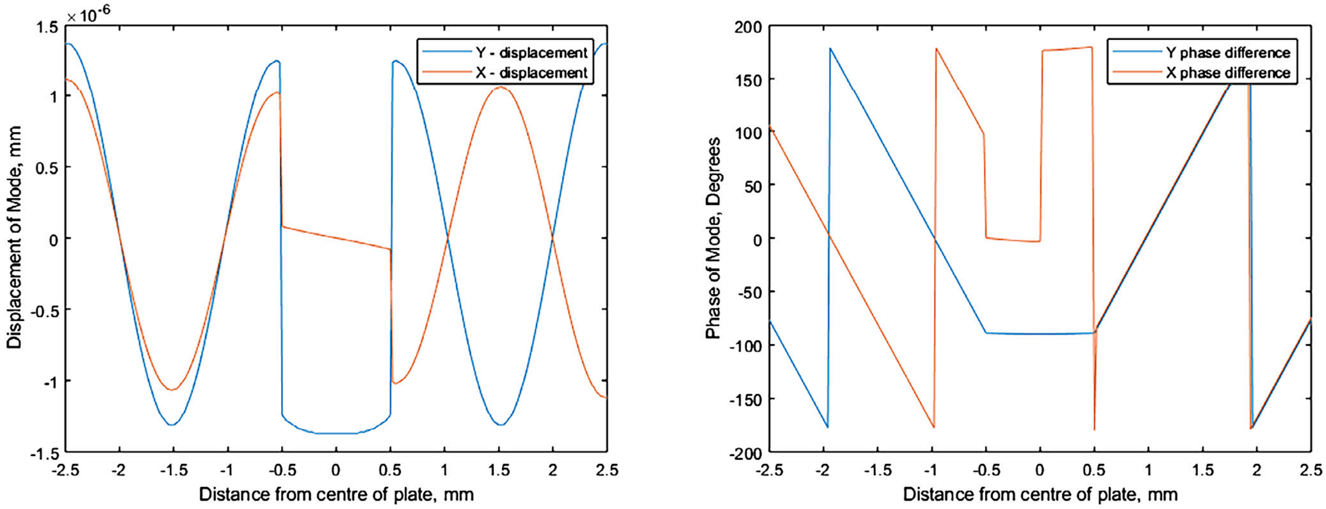

(a) Displacement data.

(b) Phase data.

Fig. 14. A0 mode shape data from Disperse for a 1 mm thick steel plate at 1 MHz submerged in water with (a) displacement (b) and phase.

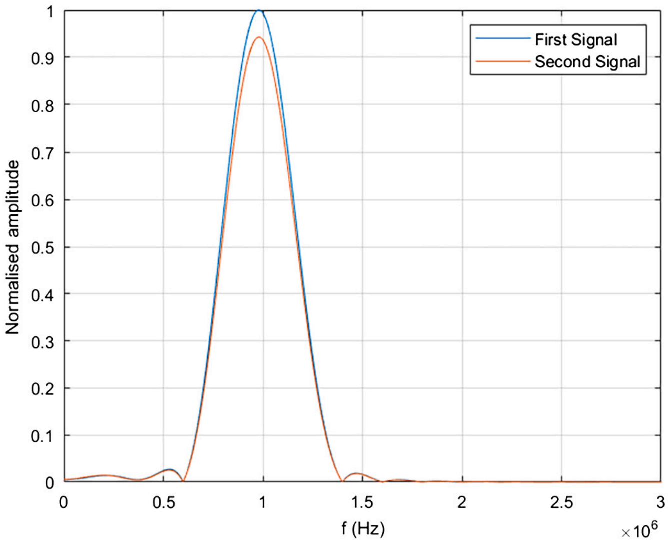

Fig. 15. FFT of first and second signal.

confirming the accuracy of the method for capturing fluid-solid wave interactions.

CRediT authorship contribution statement

Yiannis Simillides: Visualization, Validation, Software, Investigation, Conceptualization, Writing – original draft, Writing – review & editing. **Peter Huthwaite:** Funding acquisition, Methodology, Project administration, Resources, Software, Supervision, Validation, Writing – review & editing. **Michał K. Kalkowski:** Writing – review & editing, Validation, Supervision, Methodology, Project administration, Software. **Michael J.S. Lowe:** Writing – review & editing, Validation, Supervision, Software, Resources, Project administration, Methodology, Funding acquisition.

Declaration of competing interest

The authors declare that they have no known competing financial interests or personal relationships that could have appeared to influence the work reported in this paper.

Data availability

Data will be made available on request.

Acknowledgements

This work was supported by the Non-Destructive Evaluation group in Mechanical Engineering department at Imperial College London. The authors would like to thank Dr. Stewart Haslinger and Prof. Richard Craster for the discussions around the content of this paper and research in general.

References

[1] Abu-Zidan FM, Hefny AF, Corr P. Clinical ultrasound physics. J Emerg Trauma Shock 2011;4(4):501.
[2] Aggelis D, Kordatos E, Strantza M, Soulioti D, Matikas T. NDT approach for characterization of subsurface cracks in concrete. Constr Build Mater 2011;25(7):3089–97.
[3] Pavlakovic B, Lowe M, Alleyne D, Cawley P. Disperse: a general purpose program for creating dispersion curves. Rev Prog Quant Nondestruct Eval 1997:185–92.
[4] Adams SD, Craster RV, Williams DP. Two-dimensional frequency domain scattering and point excitation of partially filled elastic cylinders. J Sound Vib 2010;329(11):2147–57.
[5] Kim H-J, Song S-J, Schmerr LW. Modeling ultrasonic pulse-echo signals from a flat-bottom hole in immersion testing using a multi-Gaussian beam. J Nondestruct Eval 2004;23(1):11–9.
[6] Aristegui C, Lowe MJ, Cawley P. Guided waves in fluid-filled pipes surrounded by different fluids. Ultrasonics 2001;39(5):367–75.
[7] Skelton EA, James JH. Theoretical acoustics of underwater structures. World Scientific; 1997.
[8] Rugonyi S, Bathe K-J. On finite element analysis of fluid flows fully coupled with structural interactions. Comput Model Eng Sci 2001;2(2):195–212.
[9] Buwalda FJ, De Goede E, Knepflé M, Vuik C. Comparison of an explicit and implicit time integration method on gpus for shallow water flows on structured grids. Water 2023;15(6):1165.
[10] Huthwaite P. Accelerated finite element elastodynamic simulations using the GPU. J Comput Phys 2014;257:687–707.
[11] Faran Jr JJ. Sound scattering by solid cylinders and spheres. J Acoust Soc Am 1951;23(4):405–18.
[12] Ginzel E. NDT modelling: an overview. In: Proc. conference on modelling in non-destructive testing; 2007.
[13] Van Vossen R, Robertsson JO, Chapman CH. Finite-difference modeling of wave propagation in a fluid–solid configuration. Geophysics 2002;67(2):618–24.
[14] Cegla F, Cawley P, Lowe M. Material property measurement using the quasi-scholte mode—a waveguide sensor. J Acoust Soc Am 2005;117(3):1098–107.
[15] Dahake G, Gracewski S. Finite difference predictions of p-sv wave propagation inside submerged solids. i. Liquid–solid interface conditions. J Acoust Soc Am 1997;102(4):2125–37.
[16] Xu Y, Johnston DN, Jiao Z, Plummer AR. Frequency modelling and solution of fluid–structure interaction in complex pipelines. J Sound Vib 2014;333(10):2800–22.
[17] Villot M, Guigou C, Gagliardini L. Predicting the acoustical radiation of finite size multi-layered structures by applying spatial windowing on infinite structures. J Sound Vib 2001;245(3):433–55.
[18] Banerjee S, Kundu T. Ultrasonic field modeling in plates immersed in fluid. Int J Solids Struct 2007;44(18–19):6013–29.
[19] Goswami PP. Application of the boundary element method to coupled fluid-structure interaction problems. PhD thesis. Iowa State University; 1991.
[20] Everstine GC, Henderson FM. Coupled finite element/boundary element approach for fluid–structure interaction. J Acoust Soc Am 1990;87(5):1938–47.
[21] Yang Y, Mace BR, Kingan MJ. Wave and finite element method for predicting sound transmission through finite multi-layered structures with fluid layers. Comput Struct 2018;204:20–30.
[22] Gennaretti M, Bernardini G, Poggi C, Testa C. Velocity-potential boundary-field integral formulation for sound scattered by moving bodies. AIAA J 2018;56(9):3547–57.
[23] Bermúdez A, Rodríguez R. Finite element computation of the vibration modes of a fluid—solid system. Comput Methods Appl Mech Eng 1994;119(3–4):355–70.
[24] Belytschko T, Ong JS-J, Liu WK, Kennedy JM. Hourglass control in linear and nonlinear problems. Comput Methods Appl Mech Eng 1984;43(3):251–76.
[25] Chen HC, Taylor RL. Vibration analysis of fluid–solid systems using a finite element displacement formulation. Int J Numer Methods Eng 1990;29(4):683–98.
[26] Hamdi MA, Ousset Y, Verchery G. A displacement method for the analysis of vibrations of coupled fluid-structure systems. Int J Numer Methods Eng 1978;13(1):139–50.
[27] Bathe K, Nitikitpaiboon C, Wang X. A mixed displacement-based finite element formulation for acoustic fluid-structure interaction. Comput Struct 1995;56(2–3):225–37.
[28] Everstine G. Finite element formulatons of structural acoustics problems. Comput Struct 1997;65(3):307–21.
[29] Kalkowski MK, Muggleton JM, Rustighi E. Axisymmetric semi-analytical finite elements for modelling waves in buried/submerged fluid-filled waveguides. Comput Struct 2018;196:327–40.
[30] Cook RD, et al. Concepts and applications of finite element analysis. John Wiley & Sons; 2007.
[31] Bathe K-J, Wilson EL. Numerical methods in finite element analysis. Prentice Hall; 1976.
[32] Logg A, Mardal K-A, Wells G. Automated solution of differential equations by the finite element method: the FEniCS book, vol. 84. Springer Science & Business Media; 2012.
[33] Bathe K-J. Finite element procedures. Prentice Hall; 1996.
[34] Felippa CA. Introduction to finite element methods, vol. 885. University of Colorado; 2004.
[35] Chen L. *i*FEM: an integrated finite element methods package in MATLAB. Technical Report. University of California at Irvine; 2009.
[36] Zienkiewicz OC, Taylor RL, Zhu JZ. The finite element method: its basis and fundamentals. Elsevier; 2005.
[37] Rayleigh JWSB. The theory of sound, vol. 2. Macmillan; 1896.
[38] Courant R, Friedrichs K, Lewy H. On the partial difference equations op mathematical physics. Math Ann 1928;100(1):32–74.
[39] Belytschko T, Flanagan D, Kennedy J. Finite element methods with user-controlled meshes for fluid-structure interaction. Comput Methods Appl Mech Eng 1982;33(1–3):669–88.
[40] Golub GH, Welsch JH. Calculation of Gauss quadrature rules. Math Comput 1969;23(106):221–30.
[41] Fu Z, Lewis TJ, Kirby RM, Whitaker RT. Architecting the finite element method pipeline for the gpu. J Comput Appl Math 2014;257:195–211.
[42] Trefethen LN. Spectral methods in MATLAB. SIAM; 2000.
[43] Blackford LS, Petitet A, Pozo R, Remington K, Whaley RC, Demmel J, et al. An updated set of basic linear algebra subprograms (blas). ACM Trans Math Softw 2002;28(2):135–51.
[44] Fawzi A, Balog M, Huang A, Hubert T, Romera-Paredes B, Barekatain M, et al. Discovering faster matrix multiplication algorithms with reinforcement learning. Nature 2022;610(7930):47–53.
[45] Doolittle R, Überall H. Sound scattering by elastic cylindrical shells. J Acoust Soc Am 1966;39(2):272–5.
[46] Tamarkin P. Scattering of an underwater ultrasonic beam from liquid cylindrical obstacles. J Acoust Soc Am 1949;21(6):612–6.
[47] Pettit J, Walker A, Cawley P, Lowe M. A stiffness reduction method for efficient absorption of waves at boundaries for use in commercial finite element codes. Ultrasonics 2014;54(7):1868–79.
[48] Zienkiewicz O, Kelly D, Bettess P. The Sommerfeld (radiation) condition on infinite domains and its modelling in numerical procedures. In: Computing methods in applied sciences and engineering, 1977, I. Springer; 1979. p. 169–203.
[49] Van Pamel A, Sha G, Rokhlin SI, Lowe MJ. Finite-element modelling of elastic wave propagation and scattering within heterogeneous media. Proc R Soc, Math Phys Eng Sci 2017;473(2197):20160738.
[50] Drozdz MB. Efficient finite element modelling of ultrasound waves in elastic media. PhD thesis. Imperial College London; 2008.
[51] Cristini P, Pailhas Y, Hamon R, Xenaki A, Urso G. Influence of the sediment characteristics and of the level of burial on the acoustic response of a hollow cylinder in shallow water. In: OCEANS 2019-Marseille. IEEE; 2019. p. 1–6.
[52] Burnett D, Zampolli M. Festa: a 3-d finite element program for acoustic scattering from undersea targets. NURC Report SR, vol. 394. 2004.
[53] Alleyne D, Cawley P. A two-dimensional Fourier transform method for the measurement of propagating multimode signals. J Acoust Soc Am 1991;89(3):1159–68.
[54] Pialucha T, Guyott C, Cawley P. Amplitude spectrum method for the measurement of phase velocity. Ultrasonics 1989;27(5):270–9.
[55] Braun SG, Ewins DJ, Rao SS. Encyclopedia of vibration: FP, vol. 2. Academic Press; 2002.